Ferroelectric Switching and Electrochemistry of Pyrrole Substituted Trialkylbenzene-1,3,5-Tricarboxamides

Xiao Meng,[1] Andrey V. Gorbunov,[2] W. S. Christian Roelofs,[2] Stefan C. J. Meskers,[1] René A. J. Janssen,[1,2] Martijn Kemerink,[2,3] Rint P. Sijbesma[1]

[1]Laboratory of Macromolecular and Organic Chemistry, Eindhoven University of Technology, PO Box 513, Eindhoven, MB 5600, The Netherlands
[2]Department of Applied Physics, Eindhoven University of Technology, PO Box 513, Eindhoven, MB 5600, The Netherlands
[3]Complex Materials and Devices, Department of Physics, Chemistry and Biology (IFM), Linköping University, Linköping, SE 58183, Sweden
Correspondence to: R. P. Sijbesma (E-mail: r.p.sijbesma@tue.nl)

Received 5 December 2016; accepted 26 January 2017; published online 18 February 2017
DOI: 10.1002/polb.24318

ABSTRACT: We explore a new approach to organic ferroelectric diodes using a benzene-tricarboxamide (BTA) core connected with C10 alkyl chains to pyrrole groups, which can be polymerized to provide a semiconducting ferroelectric material. The compound possesses a columnar hexagonal liquid crystalline (LC) phase and exhibits ferroelectric switching. At low switching frequencies, an additional process occurs, which leads to a high hysteretic charge density of up to ~1000 mC/m^2. Based on its slow rate, the formation of gas bubbles, and the emergence of characteristic polypyrrole absorption bands in the UV–Vis–NIR, the additional process is identified as the oxidative polymerization of pyrrole groups, enabled by the presence of amide groups. Polymerization of the pyrrole groups, which is essential to obtain semiconductivity, is limited to thin layers at the electrodes, amounting to ~17 nm after cycling for 21 h. © 2017 The Authors. Journal of Polymer Science Part B: Polymer Physics Published by Wiley Periodicals, Inc. J. Polym. Sci., Part B: Polym. Phys. **2017**, *55*, 673–683

KEYWORDS: electropolymerization; ferroelectric liquid crystal; interface; nanomaterials; polypyrrole

INTRODUCTION Organic ferroelectrics have attracted considerable attention in the field of organic electronics during the past decade.[1] The high processability of organic materials enables a wide range of nonvolatile memory applications such as ferroelectric thin film capacitors, ferroelectric field effect transistors, and ferroelectric random access memories.[2] In combination with an (organic) semiconductor, organic ferroelectric diodes are particularly interesting for multistable electronic devices.[3,4] In the ferroelectric diode, the current can only pass through the semiconducting phase, and the charge injection into the semiconducting channel is modulated by the polarization of the ferroelectric phase.[3] In the on-state, the polarization lowers the injection barrier allowing efficient charge injection.[5,6] The injection barrier in the off-state remains constant or is even slightly higher, limiting the charge injection.[5,6]

The most successful effort toward such organic ferroelectric diodes is based on the ferroelectric–semiconductor polymer blends: poly(vinylidene fluoride-*co*-trifluoride ethylene) (P(VDF-TrFE)) and poly(3-hexylthiophene).[2,3,7,8] Advances in processing of ferroelectric-semiconducting blends has led to high remnant polarization, high programming cycle endurance, and distinct on/off states that all are important for the application of organic ferroelectric diodes.[7,9,10] However, there are also disadvantages of using polymer blends. In organic ferroelectric diodes the length scale of phase separation and morphology are hard to control, but essential for device performance.[11] Secondly, charge injection only takes place at the interface of the semiconductor and the ferroelectric, leading to relatively high resistance.[5] These challenges may be addressed by reducing the length scale at which phase separation takes place from micrometers to

Additional Supporting Information may be found in the online version of this article.

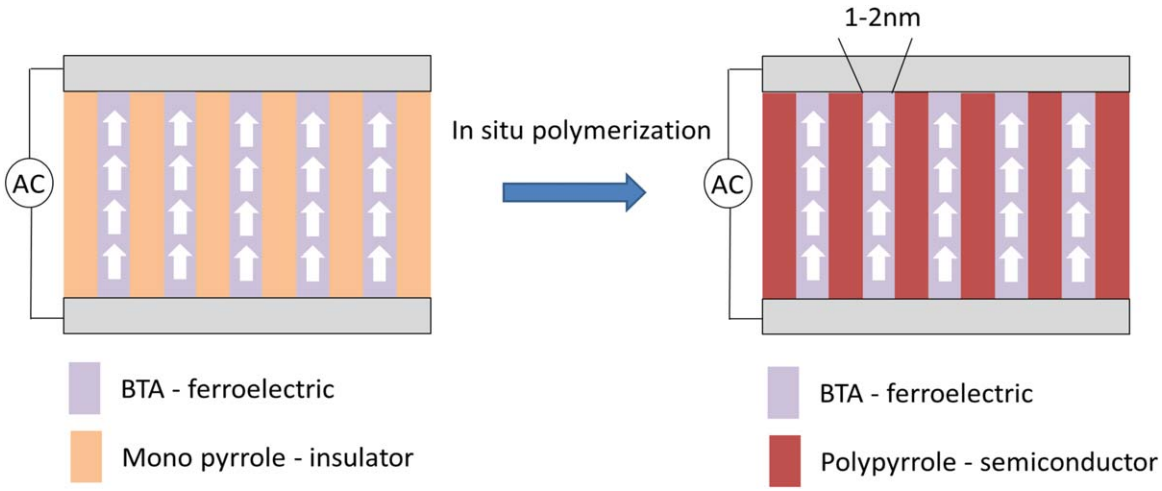

FIGURE 1 Schematic representation of the intended ferroelectric diode design. After alignment in a ferroelectric columnar mesophase, pyrrole is polymerized into quasi-1D polypyrrole channels that run parallel to the macrodipoles formed by the stacked BTA cores. [Color figure can be viewed at wileyonlinelibrary.com]

nanometers in novel materials whose molecules combine ferroelectric and semiconducting segments.

Liquid crystalline (LC) materials and composites of various types have attracted significant attention for diverse applications such as high-resolution information displays,[12,13] lasing,[14] photovoltaic devices,[15] light out-coupling,[16,17] diffraction gratings,[18,19] and so on. Columnar liquid crystals, in particular, have been used in the design of new organic ferroelectric materials.[20–26] They pose attractive opportunities to develop ferroelectric diodes, because these liquid crystals combine the molecular mobility required for long range order and alignment with the possibility to achieve microphase separation on a nanometer length scale between different parts of the mesogenic molecules.

N,*N*′,*N*″-trialkylbenzene-1,3,5-tricarboxamides (BTAs) form mesophases with a quasi-one-dimensional columnar structure via threefold hydrogen bonding between the amide groups attached to the benzene core.[25–30] The amide groups are aligned head to tail and are at an angle with the plane of the central benzene ring. The component along the columnar axis of each amide dipole has the same sign and results in a large macroscopic dipole.[25] As early as 2002, Nuckolls and coworkers noted that crowded BTAs are responsive to electric fields and have the potential to display ferroelectric properties.[31,32] Fitie´ et al. have studied two BTAs (substituted with three C10 and C18 alkyl chains) and found that the compounds have remnant polarization and coercive field in the range of 14–18 mC/m^2 and 20–30 V/μm, respectively.[25] A detailed investigation of BTAs ferroelectric switching behavior was later performed by Gorbunov et al.[33] with a combination of dielectric relaxation spectroscopy, depth-resolved pyroelectric response measurements, and classical frequency- and time-dependent electrical switching. The observation of Curie–Weiss behavior demonstrated conclusively that the BTAs are true ferroelectrics, with a Curie temperature close to the isotropic to columnar hexagonal (Col_{hex}) transition.[33] The ferroelectric properties make BTAs attractive candidates for the ferroelectric component in the design of organic ferroelectric-semiconducting materials that was discussed above.

Polypyrrole is a well-known semiconducting polymer that can be easily synthesized by either oxidative chemical or electrochemical polymerization.[34] Its conductivity can be varied over a wide range from insulating to conductive, based on the type (number, size, and position) of substituents and doping state.[35–39] The conductivity of N-substituted polypyrrole is five to six orders of magnitude lower than that of polypyrrole, because the polymer chain is forced out of planarity by the steric crowding of the substituents.[40] The conductivity decreases as substituent chain length increases.[41,42] In the undoped state, conductivity is usually below 10^{-6} S/m, low enough for use in ferroelectric diodes.[43]

In this study, we investigate the electrical properties of thin films of compound **1**, which combines the switchable macrodipole of the BTA core with three N-alkylpyrrole groups, connected via C10 alkyl chains. Compound **1** has been designed as a precursor for a semiconducting ferroelectric material formed by polymerization of the pyrrole groups (Fig. 1).

The N-substituted alkyl chains favor liquid crystallinity in a wide temperature range. We report the LC properties of compound **1**, its electric field alignment and ferroelectric switching at high frequencies. We observe large hysteretic charge density built-up at low frequencies. We compare the electrochemical behavior of **1** with two compounds that lack a LC phase, bispyrrole **5**, lacking amide dipoles, and compound **8**, which does combine pyrrole units with a benzamide dipole but lacks ferroelectric properties (Scheme 1). Using these reference compounds, we establish that the high hysteretic charge density in **1** and **8** is caused by electrochemical oxidation of the pyrrole units, which is facilitated by amide dipoles.

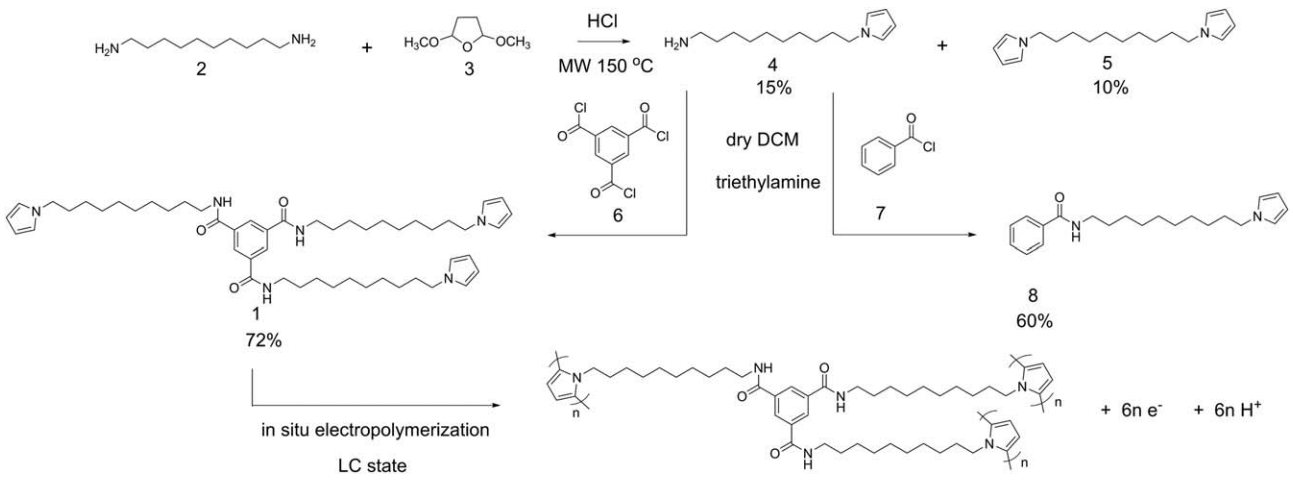

SCHEME 1 Synthesis of BTA-C10-pyrrole **1**, C10-bispyrrole **5**, benzamide-C10-pyrrole **8**, and electropolymerization of **1**.

EXPERIMENTAL

Materials

All chemicals were obtained from Aldrich or Acros and used as received. All solvents used were of AR quality or better and purchased from Biosolve. Indium tin oxide (ITO) cells with 6.8 ± 0.2 μm gap between the ITO surfaces were purchased from Instec.

Synthesis

The target compound, benzene tris-amide **1** was obtained in two steps. First, 1,10-diaminodecane **2** (1 equiv) was reacted with dimethoxy-tetrahydrofuran **3** (0.5 equiv) with HCl as catalyst via the Paal-Knorr reaction under microwave irradiation.[44] A poor yield of 1-(10-aminodecyl)pyrrole **4** (15%) was formed after 4 h. This intermediate was coupled to benzene-1,3,5-tricarboxylic acid chloride **6** to give **1** in a yield of 72% after purification. The reference molecule 1,10-bis(*N*-pyrrolyl)decane **5** was obtained by column chromatography of the crude mixture of 1-(10-aminodecyl)pyrrole **4** and *N*-(10-(1H-pyrrol-1-yl)decyl)benzamide **8** was obtained by coupling 1-(10-aminodecyl)pyrrole **4** to benzoyl chloride **7**.

Measurements

Flash chromatography was carried out using silica gel on a Reveleris flash chromatography system. NMR spectra were recorded at room temperature in $CDCl_3$ solution on a Varian Gemini 400 MHz spectrometer (400 MHz for ^{1}H NMR, 100 MHz for ^{13}C NMR). Proton chemical shifts are reported in ppm with respect to tetramethylsilane ($Si(CH_3)_4$, TMS, 0 ppm). Carbon chemical shifts are reported downfield from TMS using the resonance of $CDCl_3$ as the internal standard. MALDI-TOF-MS spectroscopy was carried out using a PerSeptive Biosystems Voyager-DE PRO spectrometer using α-cyano-4-hydroxycinnamic acid and 2-[(2E)−3-(4-tertbutylphenyl)−2-methylprop-2-enylidene]mal-ononitrile as matrices. Differential scanning calorimetry (DSC) studies were carried out in hermetic T-zero aluminum sample pans using a TA Instruments Q2000-1037 DSC equipped with a RCS90 cooling accessory. The thermal transitions were studied mainly on the first cooling and second heating with the rate of 10 °C/min. Polarized optical microscopy (POM) was performed on a Leica CTR 6000 microscope equipped with two crossed polarizers, a Linkam hot-stage THMS600 as the sample holder, a Linkam TMS94 controller and a Leica DFC420 C camera. UV–Vis–NIR measurements were performed on a PerkinElmer Lambda 900 UV–Vis–NIR spectrophotometer. X-ray diffraction (XRD) studies were conducted using a Ganesha lab instrument equipped with a GeniXCu ultralow divergence source producing X-ray photons with a wavelength of 1.54 Å and a flux of 1×10^8 photons/s. Diffraction patterns were collected on a Pilatus 300K silicon pixel detector with 487×619 pixels of 172 μm^2 in size. Glass capillaries were filled with the material for the diffraction analysis and placed in a Linkam HFSX350 heating stage and measured at a range of −80 °C to +160 °C with 10 °C/min. Each pattern was recorded for 10 min. Fabrication of thin-film metal–insulator–metal devices was done by thermal deposition of ~100 nm Al through a shadow mask on a glass plate as bottom electrode. The organic material was then spin coated after which the top Al contact (100 nm) was evaporated through the same shadow mask, rotated by 90°, defining the active area as the overlap between the top and bottom electrodes. The current voltage measurement took place inside a Janus probe station at atmospheric pressure. Switching signal waveforms were applied by an Agilent 33120a arbitrary waveform generator and amplified by a Falco WMA-300 high voltage amplifier. The actual circuit current was measured by a Keithley 6485 picoammeter and visualized and stored on an Agilent DSO7104A oscilloscope for further analysis.

RESULTS

Liquid Crystallinity

C10-bispyrrole **5** is a simple molecule that contains two pyrrole moieties but has no amide dipoles. At room temperature, the material is an isotropic oil and has no LC phase. Benzamide-C10-pyrrole **8** is a molecule that does have an amide bond in addition to a pyrrole group. It is a crystalline material with an isotropic melting point of 75 °C. In contrast to these reference compounds, BTA derivative **1** has a

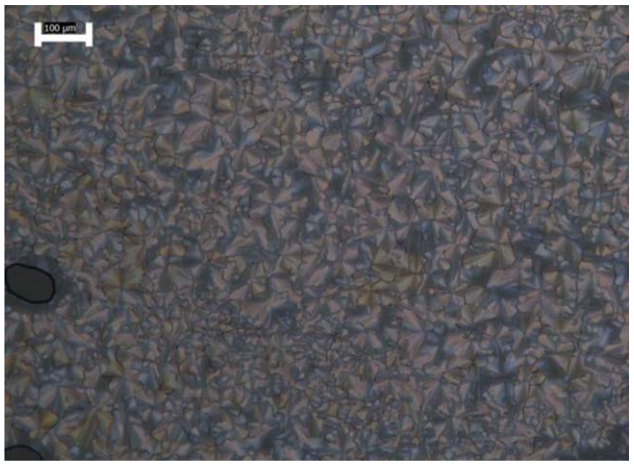

FIGURE 2 POM micrograph of BTA-C10-pyrrole (**1**) at 80 °C after cooling back from the isotropic temperature of 127 °C. Scale bar = 100 μm. [Color figure can be viewed at wileyonlinelibrary.com]

mesophase up to 127 °C as observed with POM. Figure 2 shows the optical texture obtained by POM at 80 °C upon cooling down from isotropic temperature at a rate of 10 °C/min. Under crossed polarizers, the material showed a birefringent focal conic texture indicating a hexagonal columnar structure.

The thermal behavior of compound **1** was studied further with DSC. The phase transition temperatures and enthalpies were determined from the first cooling and second heating trace. Upon heating, the LC to isotropic phase transition takes place at 127 °C (transition enthalpy is 3.21 J/g), while on cooling, the LC phase transition occurs at 120 °C (transition enthalpy is 4.13 J/g). No additional phase transition was observed when cooling down further to −50 °C, indicating the LC phase is stable over a wide temperature range (Supporting Information S1). To confirm the hexagonal

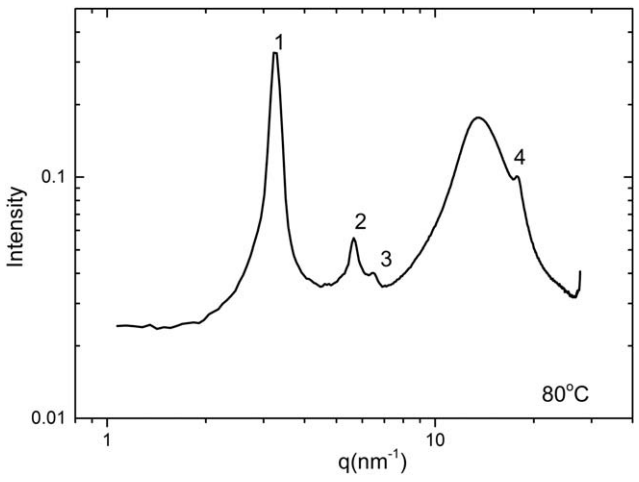

FIGURE 3 X-ray scattering pattern of BTA-C10-pyrrole (**1**) measured at 80 °C.

TABLE 1 XRD Data of BTA-C10-Pyrrole (1) at 80 °C

Peak	q (nm^{-1})	hkl	d_{obs} (nm)	d_{cal} (nm)	Parameter
1	3.24	100	1.94	1.94	Col_{hex}
2	5.63	110	1.12	1.12	$a = 2.24$ nm
3	6.48	200	0.97	0.97	$c = 0.35$ nm
4	17.80	001	0.35	0.35	

arrangement, wide angle X-ray scattering (WAXS) was studied. The X-ray scattering pattern at 80 °C is shown in Figure 3. In the small angle regime there are three distinct equatorial reflection peaks at 3.24 nm^{-1}, 5.63 nm^{-1}, and 6.48 nm^{-1}, respectively, corresponding to the lattice distances $d[100] = 1.94$ nm, $d[110] = 1.12$ nm, and $d[200] = 0.97$ nm. The reciprocal spacing ratio of $1:\sqrt{3}:2$ in q-space of these three peaks is consistent with a Col_{hex} mesophase. In the wide angle regime, the broad diffuse halo corresponds to the liquid-like alkyl chains and the reflection at 17.8 nm^{-1}, with a d-spacing of 0.35 nm, has a value typical of the

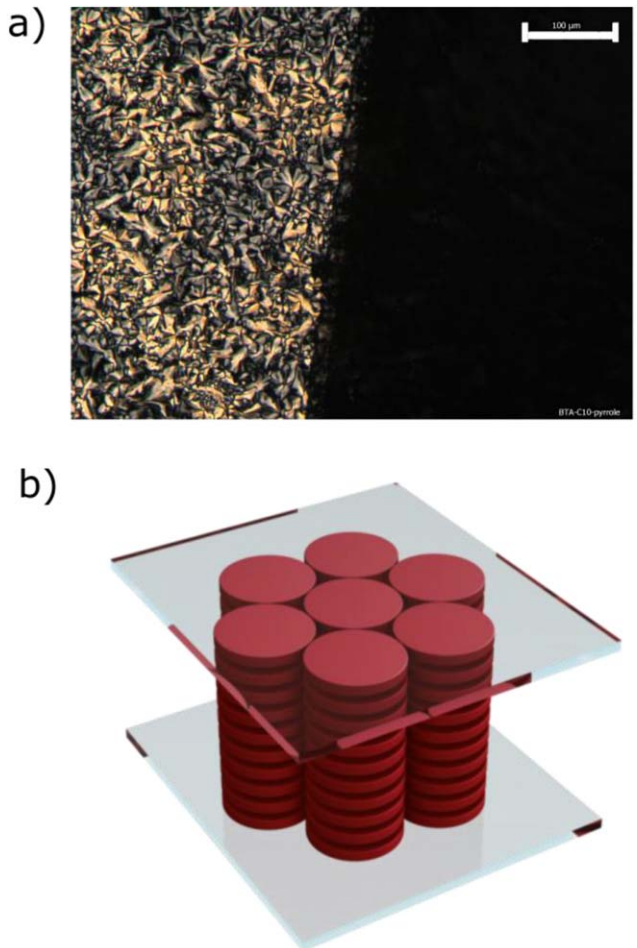

FIGURE 4 (a) POM image of homeotropically aligned in electrode area (right) and nonaligned (left) BTA-C10-pyrrole (**1**), scale bar = 100 μm. (b) Schematic illustration of the molecular packing after homeotropic alignment. [Color figure can be viewed at wileyonlinelibrary.com]

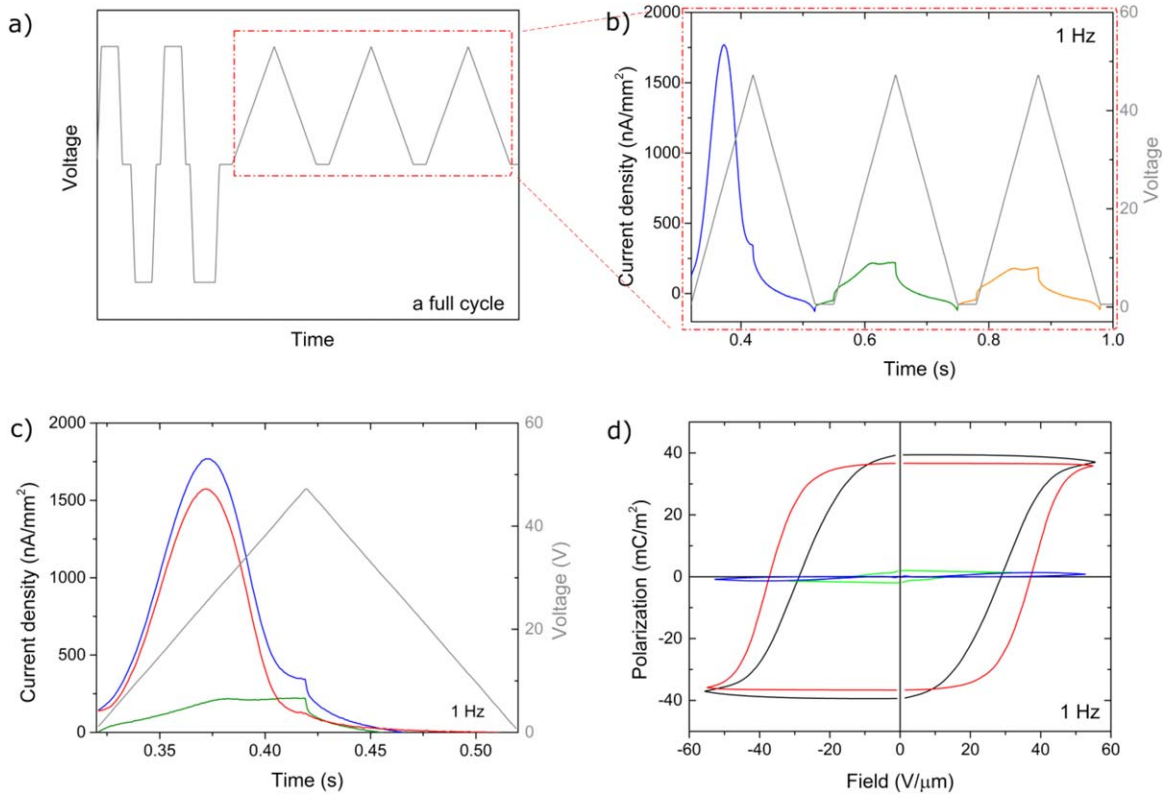

FIGURE 5 (a) A single cycle of the voltage wave form used for probing the hysteretic polarization. (b) Current response to the triple triangular wave at 1 Hz. The maximum voltage corresponds to a field $E = 53$ V/μm. (c) The current associated with the polarization reversal (red) was obtained by subtracting the background current (green) from the raw signal (blue). (d) *P–E* hysteresis loops of BTA-C10-pyrrole **1** (black line, Al contacts, device thickness 850 nm, 53 V/μm), BTA-C10-alkyl (red line, Al contacts, device thickness 1400 nm, 53 V/μm), C10-bispyrrole **5** (blue line, ITO contacts, device thickness 6500 nm, 53 V/μm), and benzamide-C10-pyrrole **8** (green line, ITO contacts, device thickness 6500 nm, 37 V/μm), at 80 °C, and 1 Hz. [Color figure can be viewed at wileyonlinelibrary.com]

interdiscotic distance of ordered BTAs.[28, 45–47] Details of the *d*-spacings and lattice parameters for the hexagonal structure of **1** are reported in Table 1.

Homeotropic alignment of the LC phase of **1** was obtained by applying an external electric field between ITO electrodes. First, a commercial 25 mm^2 glass cell with a gap of 6.8 μm and ITO electrodes was filled with **1** by capillary force, heating the material to its isotropic phase at $T = 150$ °C. An electric field of 20 V/μm was then applied to the device at 110 °C. After 5 min, the material in the ITO-covered central part of the cell became transparent under normal illumination while it was dark under crossed polarizers, indicating homeotropic alignment. In contrast, the field-free glass area of the cell remained birefringent with a focal conic texture corresponding to nonhomeotropic alignment [Fig. 4(a)].

Polarization at High Frequencies

The investigation of polar switching behavior was studied on electric field aligned samples between Al electrodes. A specific voltage pattern was applied in the measurements, see Figure 5(a). The first two block waves have an amplitude that significantly exceeds the coercive field and were used to erase any previous polarization state and bring the device in a negative polarization state. The current response to the following triangular waves shown in Figure 5(b) is used to obtain the ferroelectric hysteresis loop. At frequencies around or above 1 Hz, the plot of current density versus time displayed a single peak corresponding to a polar switching process, see Figure 5(c). The response also contains a background current due to intrinsic conductive and capacitive effects of the material as well as leakage.[25] As polarization reversal only takes place during the first upward sweep, the current response to the second and third triangular waves represent a background signal. The "true" switching current response induced by polar switching (red line) is obtained by subtracting the background (green line) from the signal peak (blue line). By integrating the corrected current response versus time and using the known film thickness and electrode area,[25,33] the electric displacement (D) which is calculated as the charge density was obtained. In most cases, for high permittivity ferroelectric materials without free charge carriers, the charge density is nearly equivalent to the ferroelectric polarization (P). Polarization is plotted as a function of the electric field showing a *P–E* hysteresis loop in Figure 5(d, black line). The plot shows a clear ferroelectric switching behavior with a remnant polarization (P_r) of 39 mC/m^2 and a coercive field (E_c) of 30 V/μm.

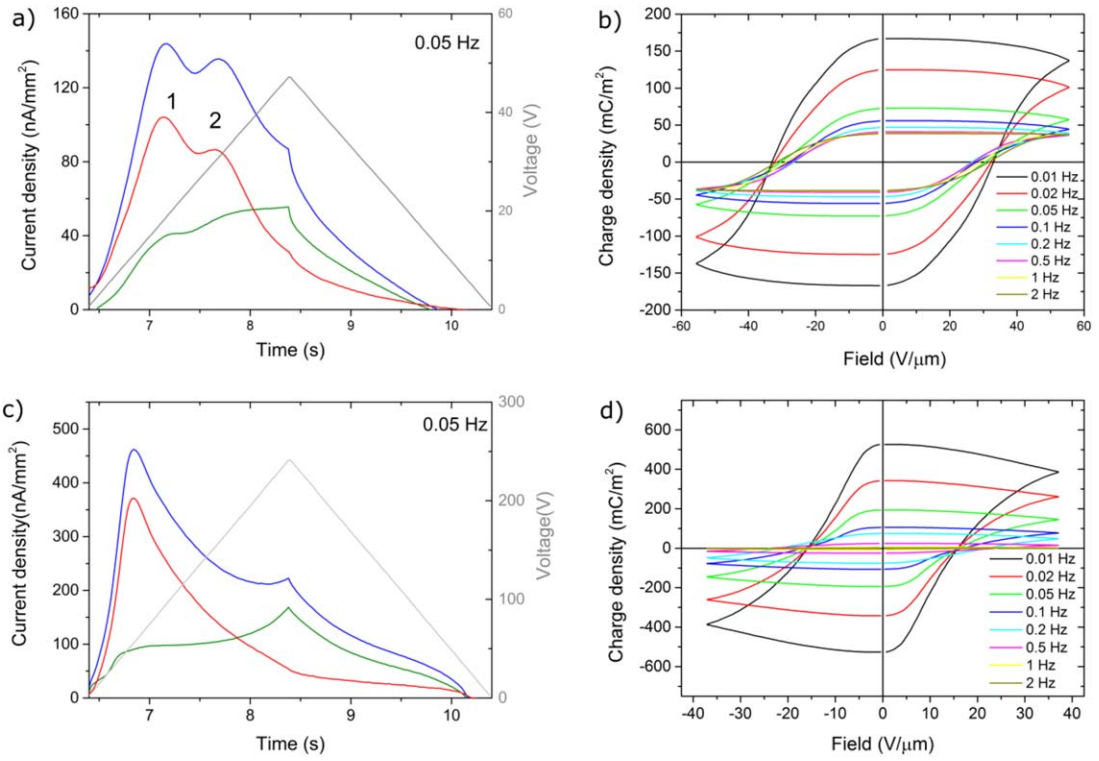

FIGURE 6 (a) Current density as a function of time at 0.05 Hz of **1** showing two processes labeled 1 and 2. Blue line: raw signal, green line: background signal, red line: corrected signal. (b) Hysteretic charge density-field hysteresis loops of **1** at 80 °C from 0.01 to 2 Hz (Al contacts, device thickness 850 nm, 53 V/μm). (c) Current density as a function of time at 0.05 Hz of **8** showing only a single peak associated with a high hysteretic charge density. Blue line: raw signal, green line: background signal, red line: corrected signal. (d) Hysteretic charge density-field hysteresis loops of **8** at 80 °C from 0.01 to 2 Hz (ITO contacts, device thickness 6500 nm, 37 V/μm). [Color figure can be viewed at wileyonlinelibrary.com]

For comparison, the hysteresis loop of BTA-C10-alkyl is shown as a red solid line in Figure 5(d). BTA-C10-alkyl lacks pyrrole groups and its ferroelectric properties have been studied in detail.[25,26,33] The ferroelectric parameters of BTA-C10-pyrrole **1** are very similar to those of BTA-C10-alkyl [black and red line in Fig. 5(d)].

Theoretical studies have shown that in columnar stacks, all amide groups align, resulting in molecular dipole moments in the order of 9-14 Debye.[28, 48–50] The comparable polarization in BTA-C10-pyrrole **1** and BTA-C10-alkyl establish that the presence of polymerizable pyrrole side groups does not affect the ability of the BTA core to organize in a field-aligned hexagonal columnar LC mesophase with ferroelectric behavior.

Negligible polarization signals were observed in compound **5** and **8** (blue and green lines in Figure 5(d), indicating that these materials are not ferroelectric, as expected for isotropic liquids, and in the case of **5**, the absence of dipoles from amide groups.

High Charge Density at Low Frequencies

When the frequency was decreased below 1 Hz (0.5–0.01 Hz), an additional transient current peak appeared in the current density plot of **1** [Fig. 6(a)]. In these experiments, the charge density not only consists of ferroelectric polarization but also another process. Integration of the transient current peaks of **1** results in a high hysteretic charge density that increases with decreasing frequency, reaching 170 mC/m^2 at 0.01 Hz for **1**, see Figure 6(b). In a mixture with BTA-C10-alkyl (80 wt % BTA-C10-pyrrole) which has lower viscosity, the value of the hysteretic charge density reached up to ~1000 mC/m^2 at 0.01 Hz, ~25 times higher than the polarization induced by dipolar switching at higher frequencies indicating a new process occurs. Although the high hysteretic charge density only occurred when the field was above the coercive field, these values are too high to be the result of switching of amide electric dipoles. Significantly, a single transient current peak was also observed for the non-ferroelectric compound **8** at low frequencies, leading to a high hysteretic charge density [Fig. 6(c,d)]. No polarization corresponding to polar switching is observed in **5** at any frequency (Supporting Information S9). The appearance of transient currents at low frequency observed in **1** (containing amide dipoles, pyrrole groups and having ferroelectricity) and **8** (containing amide dipoles and pyrrole groups but lacking ferroelectricity), but not in compound **5** (containing pyrrole groups but lacking amide dipoles) or BTA-C10-alkyl (containing amide dipoles but lacking pyrrole groups) shows

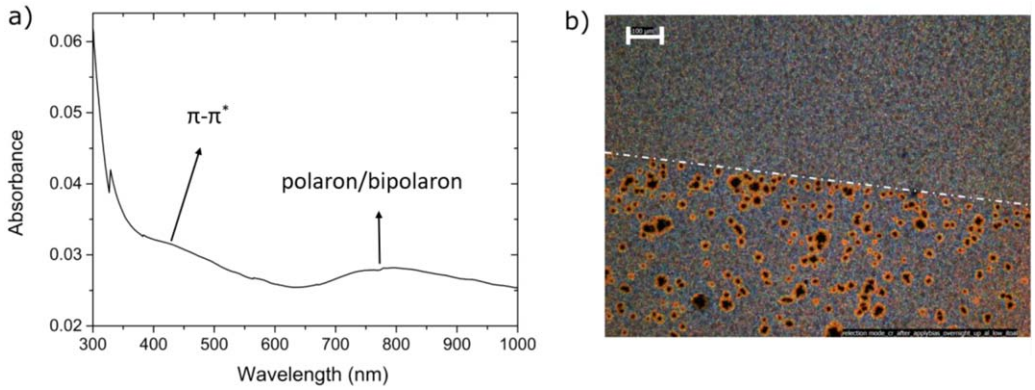

FIGURE 7 (a) UV–Vis–NIR spectrum of BTA-C10-pyrrole material in ITO–Al device after applying a cyclic bias for 2 h and subsequent etching of the Al electrode. (b) Polarized optical microscopy image of the BTA-C10-pyrrole material on ITO after removal of the Al electrode in both the active region (lower half) and the nonactive region (upper half) of the diode. Scale bar = 100 μm. [Color figure can be viewed at wileyonlinelibrary.com]

that the process which is observed in **1** and **8** requires both amide groups and pyrrole groups.

As even full alignment of amide dipoles cannot account for the high hysteretic charge density, we propose that the effect is the result of a transient current upon each reversal of polarity, caused by an anodic and a cathodic electrochemical process in combination with transport of charge carriers through the material. The presence of a second, nonferroelectric process is consistent with the fact that the high hysteretic charge density in Figure 6(b,d) continues to increase upon decreasing the sweep rate. For BTA-C10-alkyl and compound **1** at high frequency [Fig. 5(d)] this behavior is negligible. In the remaining part of this section we describe experiments that shed further light on the nature of the electrochemical processes and the charge carriers.

Electrode Processes

To further identify processes taking place at the electrodes in the low-frequency process, thin film devices with one Al and one ITO electrode were cycled at low frequencies for several hours. Figure 7(a) shows the UV–Vis spectrum of a thin film of compound **1** between an Al and an ITO electrode after cycling for 2 h (80 °C, 53 V/μm triangular wave voltage, $f = 0.01$ Hz). Two absorption peaks are present at 440 nm and 800 nm which are in line with the π–π^* interband and polaron/bipolaron band of polypyrrole, suggesting that the proposed electrochemical process is the formation of doped polypyrrole by anodic oxidation. Figure 7(b) shows a POM image of the film observed in transmission mode from the Al-side after removal of the Al electrode by washing with aqueous HCl. In contrast to the Al region without electric field, the Al-ITO region showed many holes of a few micrometers in size that can be ascribed to the formation of gas bubbles.

Charge Carrier Mobility

To further study the mobility of charges generated in the electrochemical process at low frequencies, a mixture of BTA-C10-pyrrole with BTA-C10-alkyl (80 wt % BTA-C10-pyrrole) was used. The current response to a block wave was measured on films of different thicknesses, 0.24 μm, 0.38 μm, 0.65 μm, and 1.3 μm, respectively, at a temperature of 80 °C. Figure 8 shows the current response of the mixture as a function of time at 0.02 Hz. In all samples a sharp peak was observed within ~1 s after a field was applied, corresponding to dipolar switching. Following the dipolar switching peak, a broad peak was observed with a maximum that moves to longer times with increasing film thickness, behavior that is expected for electric field induced displacement of mobile charge carriers, for example, protons. Taking the peak maxima at ~2–7 s as a measure for the transit time, we estimate the associated mobility to be $\sim 2 \times 10^{-11}$ cm^2/V s. For proton conducting materials incorporating imidazole groups, the proton mobility at elevated temperature (80 °C) can be estimated at 10^{-8} cm^2/V s.[51] As can be expected, the proton mobility in our system, with the weaker pyrrole proton acceptor, is lower than the mobility in the imidazole system.

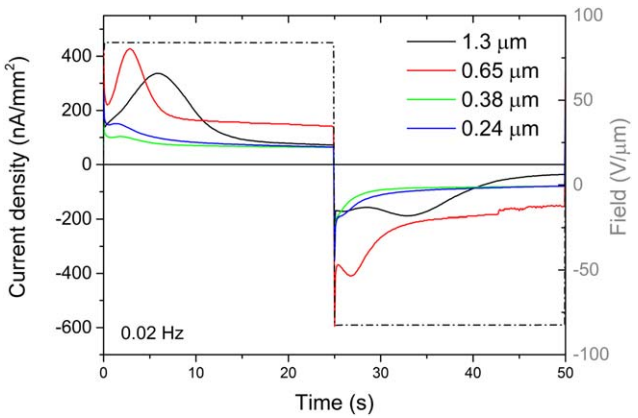

FIGURE 8 Current density as a function of time for BTA-C10-pyrrole/BTA-C10-alkyl mixture (80 wt % BTA-C10-pyrrole) thin films of different thickness in response to a 0.02 Hz block wave with an amplitude of 83 V/μm at 80 °C. [Color figure can be viewed at wileyonlinelibrary.com]

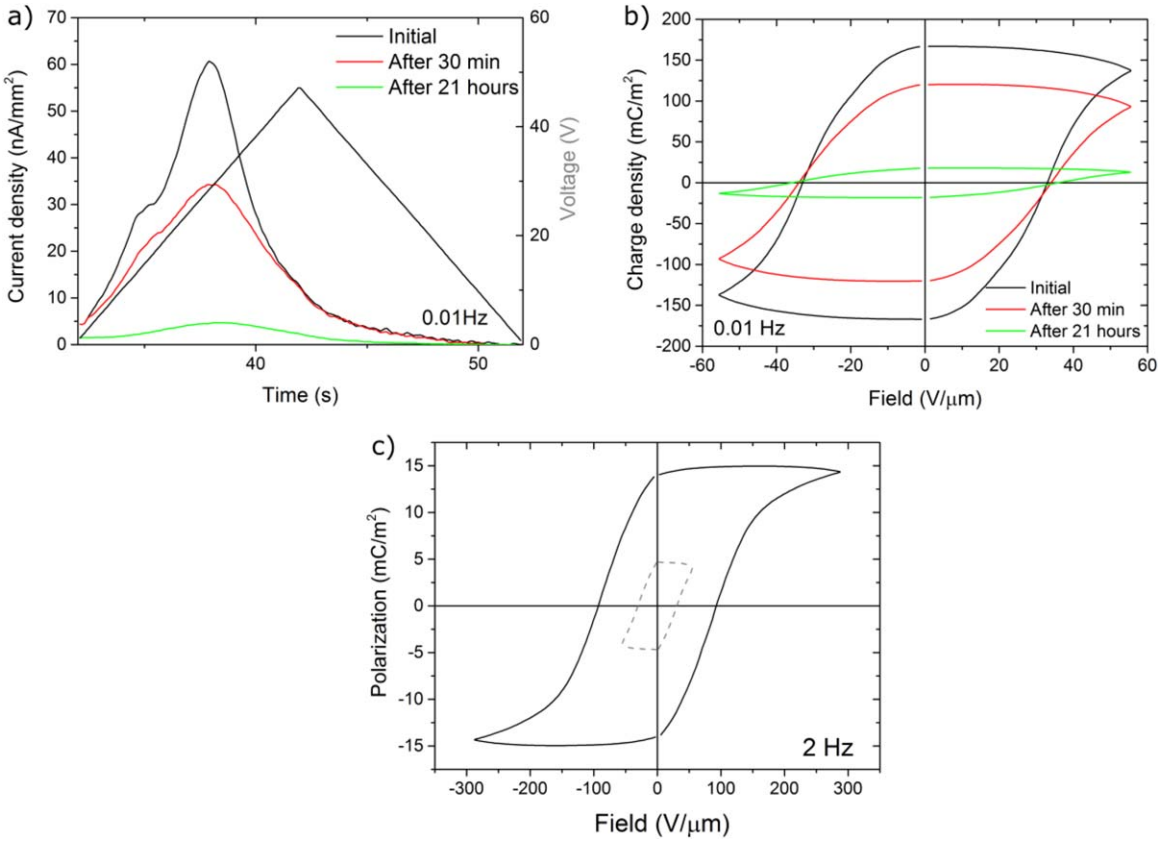

FIGURE 9 (a) Corrected current density as a function of time for BTA-C10-pyrrole thin films after different cycling times and (b) corresponding hysteretic charge density-field loops. Black line: pristine, red line: after 30 min, green line: after 21 h of **1** upon cycling at 0.01 Hz, drive amplitude 53 V/μm. (c) *P–E* loops probed at normal (dashed line, 53 V/μm) and high field (solid line, 287 V/μm) at 2 Hz after cycling for 21 h at 53 V/μm. [Color figure can be viewed at wileyonlinelibrary.com]

Both the polar switching and the low frequency electrical displacement decrease with time under continuous bias cycling, for example, using the cycle of Figure 5(a). Independent of probe frequency, the polar switching peak decreased with time as shown in Figure 9(a,b). After 21 h, the first (polar) switching peak had decreased from 39 to 5 mC/m^2, showing very weak ferroelectric switching behavior under a field of 53 V/μm [dashed line in Fig. 9(c)]. The second peak, associated with the hysteretic charge density decreased dramatically from 170 mC/m^2 to 30 mC/m^2. A similar decrease of hysteretic charge density was also observed in **8** upon cycling.

A very weak ferroelectric response of 5 mC/m^2 was still observed at 2 Hz after 21 h continuous bias cycling under a field of 53 V/μm. When a stronger field was applied, the material again displayed distinct polar switching, with a remnant polarization of 15 mC/m^2 and a higher coercive field of 90 V/um as shown in panel (c) of Figure 9. In another device, which was cycled for 24 h under a field of 53 V/μm, ferroelectric switching behavior could also be revived by application of a high field, leading to a remnant polarization of 6 mC/m^2 and a coercive field of to 133 V/μm. The diminishing charge density [at 0.01 Hz, Fig. 9(b)] and reduced polarization [at 2 Hz, Fig. 9(c)] are indicative of strong suppression of electrochemical oxidation and ferroelectric switching, respectively. Charge density and polarization in these experiments should be regarded as "effective" device parameters and not as material parameters as will be further discussed later.

DISCUSSION

The experiments on thin films of **1** demonstrate that the material shows ferroelectric switching upon applying a field of sufficient strength. In addition, at low frequencies, a second process leads to extremely high hysteretic charge density of up to ~1000 mC/m^2. In this section we will discuss this second process.

Next to the high charge density, we observed the second process with a slow rate, the UV–Vis–NIR spectrum of films after prolonged cycling showing a polypyrrole absorption band and the formation of gas bubbles. These observations are all consistent with the production of protons during the electrochemical oxidation of pyrrole groups, which may be reduced to hydrogen gas at the opposite electrode. Pyrrole oxidation produces radical cations.[52] Coupling of two radical cations results in the formation of a pyrrole dimer by the loss of

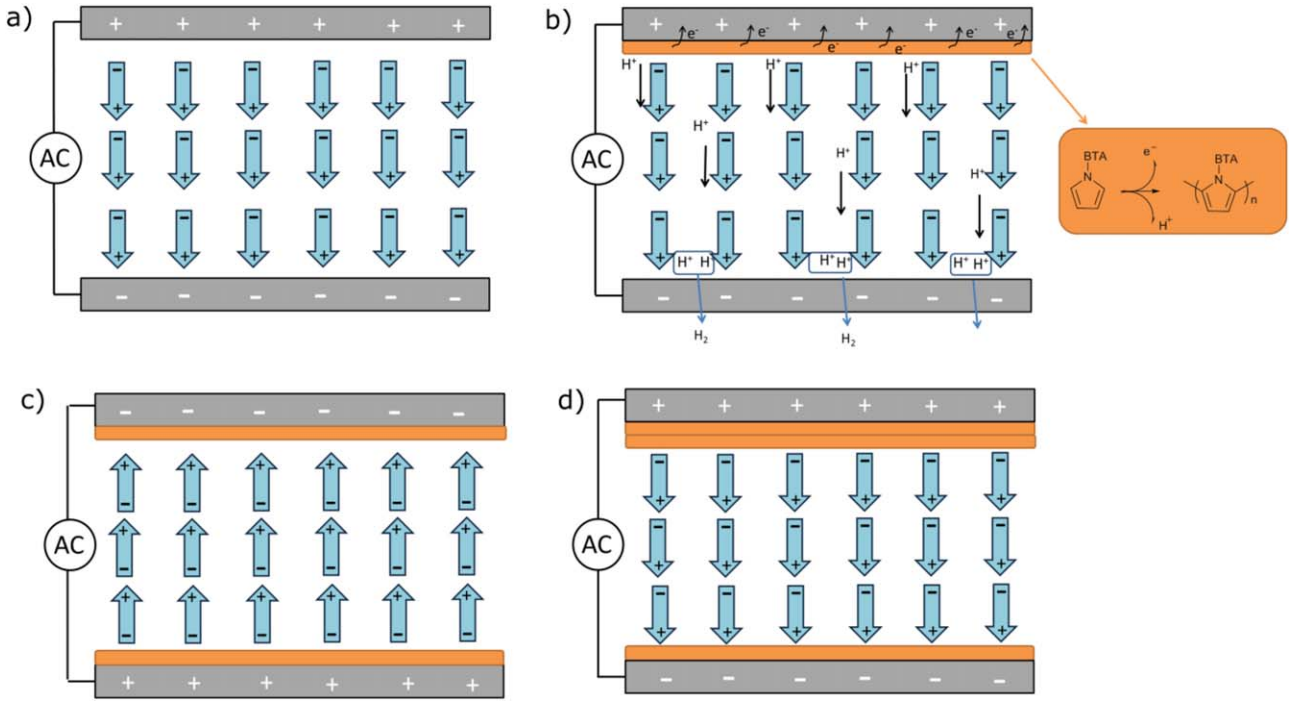

FIGURE 10 Schematic illustration of ferroelectric switching and electrochemical reaction of BTA–pyrrole material under bias stress. (a) First, the amide dipoles are oriented by the electric field. (b) The negative charges of the dipoles reduce the electron injection barrier from the material into the electrode which facilitates the electrochemical oxidation of pyrrole. During pyrrole polymerization, protons are produced and a thin layer of polypyrrole is formed at the interface. The protons move to the opposite electrode by the electric field and reduce there to hydrogen gas. (c) During cycling, pyrrole oxidation takes place at both electrodes. (d) Multiple polypyrrole layers are formed upon cycling. [Color figure can be viewed at wileyonlinelibrary.com]

two protons (Scheme 1). The polymerization continues by reoxidation of the dimer (or oligomers), loss of protons, and recoupling. Under influence of the electric field the protons move to the negative electrode where they accumulate and give rise to high charge densities that counteract the applied field. If reduction of the protons to hydrogen is slower than their production, protons accumulate and the process terminates when the internal field is completely screened. Under those conditions we expect the current to be a transient, like it was observed in thin films of **1** (Fig. 8).

Comparison of the presence of the slow process in the different materials studied shows that the oxidation of pyrrole units depends on the presence of amide groups in the molecule, but does not require ferroelectricity, as the slow process is absent in **5**, but is present in a film of non-ferroelectric liquid **8**. A potential effect of amide groups is that their electric field induced orientation is enough to reduce the electron injection barrier from the material into the electrode. Dipole facilitated charge injection was recently used to enhance water oxidation at Si-based photoanodes and could also facilitate the electrochemical oxidation of pyrrole at the electrode interface.[53] In absence of dipolar effects the potential drop in the injection layer of our device would only amount to 0.05 eV for a 1 nm injection layer at a typical maximum bias of 250 V in a homogenous field across a 5 μm thick film. Depending on the actual potential drop, facilitation of charge injection similar to that in Si-based photoanodes may also be operative in our devices. Regardless of any barrier modulation, the presence of amide groups may facilitate proton transport, as has been observed in acid-doped polyamides.[54]

Due to the alternation of the polarity of the applied field during cycling, pyrrole oxidation takes place at both electrodes, and gradually a thin layer of polypyrrole is formed at both interfaces. The formation of hydrogen gas bubbles reduces the interfacial area between the electrodes and the organic layer. The decrease in hysteretic charge density over time can be ascribed to a combination of these two effects. Likewise, the presence of poorly conductive or "dead" interfacial layers is well known to suppress ferroelectric switching, again in agreement with the observations in Figure 9.[55]

The combination of ferroelectric switching and electrochemical polymerization in the BTA-pyrrole system is schematically illustrated in Figure 10. Initially, panel (a), the amide dipoles are oriented by the electric field. The oriented amide groups at the interface reduce the electron injection barrier from the material into the electrode which facilitates the electrochemical oxidation of pyrrole, see panel (b). A thin layer of polypyrrole is formed, and protons are produced during polymerization. By the driving force of the electric field, protons move to the other electrode and reduce to

hydrogen gas. During cycling, pyrrole oxidation takes place at both electrodes and polypyrrole layers are formed gradually upon cycling (panels (c, d)).

An estimate of the amount of polypyrrole formed in each cycle can be obtained from the observed current, showing that at 0.01 Hz under a field of 53 V/μm, two cycles generate a single monolayer. That means that for the experiment in Figure 9 ~2 and ~100 layers will have formed after 30 min and 21 h of cycling at 0.01 Hz, respectively.[56] This is consistent with a minor respectively a strong suppression of both the ferroelectric and electrochemical oxidation signals.

CONCLUSIONS

We have synthesized and characterized a columnar liquid crystal BTA-C10-pyrrole combining both ferroelectric and electrochemical behavior. At high frequencies, the material shows ferroelectric switching behavior similar to BTA without the pyrrole groups, which is a true ferroelectric material. At low frequencies, however, extremely high hysteretic charge density is measured, which is ascribed to electrochemical polymerization of pyrrole groups, in combination with cathodic reduction of protons, coupled with proton transport across the film.

The observed electrochemical polymerization of BTA-C10-pyrrole represents a direct approach to materials for organic ferroelectric diodes in which the ferroelectric and semiconducting components are mixed on a nanoscale. This length scale is much smaller than that in microphase separated blends of P(VDF-TrFE) with a semiconducting polymer. However, a number of limitations of the current system need to be addressed for successful development of this concept. The experimental data support the formation of at most a thin film of polypyrrole at the electrode surfaces. Thus, our intended goal of a ferroelectric material with nanophase separated domains of semiconducting material has only partly been achieved, with a polymerization that is limited to a thicknesses of a few tens of nm. For the formation of ferroelectric diodes with a continuous semiconducting phase, chemical polymerization of pyrrole groups may be employed, which results in polypyrrole in a doped state. However, chemical polymerization of the material to form an operating device requires a complex sequence of steps, consisting of electric field alignment; electrode removal; chemical polymerization; electrode deposition. An alternative method of introducing the semiconducting component that we will explore in the future is to make use of hydrogen bonded stacks of aromatic units with high charge carrier mobility.

ACKNOWLEDGMENTS

This work is part of the research programme NWOnano with project number 11512, which is (partly) financed by the Netherlands Organisation for Scientific Research (NWO) and is supported by the Ministry of Education, Culture and Science (Gravity program 024.001.035).

REFERENCES AND NOTES

1 S. Horiuchi, Y. Tokura, *Nat. Mater.* **2008**, *7*, 357–366.

2 R. C. G. Naber, K. Asadi, P. W. M. Blom, D. M. de Leeuw, B. de Boer, *Adv. Mater.* **2010**, *22*, 933–945.

3 K. Asadi, D. M. de Leeuw, B. de Boer, P. W. M. Blom, *Nat. Mater.* **2008**, *7*, 547–550.

4 J. Lee, A. J. J. M. van Breemen, V. Khikhlovskyi, M. Kemerink, R. A. J. Janssen, G. H. Gelinck, *Sci. Rep.* **2016**, *6*, 24407.

5 M. Kemerink, K. Asadi, P. W. M. Blom, D. M. de Leeuw, *Org. Electron.* **2012**, *13*, 147–152.

6 K. Asadi, T. G. de Boer, P. W. M. Blom, D. M. de Leeuw, *Adv. Funct. Mater.* **2009**, *19*, 3173–3178.

7 K. Asadi, M. Li, P. W. M. Blom, M. Kemerink, D. M. de Leeuw, *Mater. Today.* **2011**, *14*, 592–599.

8 R. C. G. Naber, J. Massolt, M. Spijkman, K. Asadi, P. W. M. Blom, D. M. D. Leeuw, *Appl. Phys. Lett.* **2007**, *90*, 113509.

9 C. R. McNeill, K. Asadi, B. Watts, P. W. M. Blom, D. M. de Leeuw, *Small* **2010**, *6*, 508–512.

10 J. C. Scott, L. D. Bozano, *Adv. Mater.* **2007**, *19*, 1452–1463.

11 K. Asadi, H. J. Wondergem, R. S. Moghaddam, C. R. McNeill, N. Stingelin, B. Noheda, P. W. M. Blom, D. M. de Leeuw, *Adv. Funct. Mater.* **2011**, *21*, 1887–1894.

12 T. Uchida, *Jpn. J. Appl. Phys.* **2014**, *53*, 03CA02.

13 S. S. Gandhi, M. S. Kim, J. Y. Hwang, L. C. Chien, *Adv. Mater.* **2016**, *28*, 8998–9005.

14 S. Yokoyama, S. Mashiko, H. Kikuchi, K. Uchida, T. Nagamura, *Adv. Mater.* **2006**, *18*, 48–51.

15 K. Sun, Z. Xiao, S. Lu, W. Zajaczkowski, W. Pisula, E. Hanssen, J. M. White, R. M. Williamson, J. Subbiah, J. Ouyang, A. B. Holmes, W. W. H. Wong, D. Jones, *J. Nat. Commun.* **2015**, *6*, 6013.

16 S. S. Gandhi, L. C. Chien, *Opt. Mater.* **2016**, *54*, 300–305.

17 S. S. Gandhi, L. C. Chien, *SID Symp. Dig. Tech. Pap.* **2016**, *47*, 1662–1665.

18 F. Peng, Y. H. Lee, Z. Luo, S. T. Wu, *Opt. Lett.* **2015**, *40*, 5097.

19 L. Weng, S. H. Lee, L. C. Chien, *SID Symp. Dig. Tech. Pap.* **2015**, *46*, 1552–1554.

20 F. Araoka, H. Takezoe, *Jpn. J. Appl. Phys.* **2014**, *53*, 01AA01.

21 H. Takezoe, F. Araoka, *Liq. Cryst.* **2014**, *41*, 393–401.

22 K. Kishikawa, S. Nakahara, Y. Nishikawa, M. Natsukawa, S. Kohmoto, *Mol. Cryst. Liq. Cryst.* **2009**, *498*, 11–18.

23 F. A. Daigo Miyajima, *Science* **2012**, *336*, 209–213.

24 K. Kishikawa, S. Nakahara, Y. Nishikawa, S. Kohmoto, M. Yamamoto, *J. Am. Chem. Soc.* **2005**, *127*, 2565–2571.

25 C. F. C. Fitié, W. S. C. Roelofs, P. C. M. M. Magusin, M. Wübbenhorst, M. Kemerink, R. P. Sijbesma, *J. Phys. Chem. B.* **2012**, *116*, 3928–3937.

26 C. F. C. Fitié, W. S. C. Roelofs, M. Kemerink, R. P. Sijbesma, *J. Am. Chem. Soc.* **2010**, *132*, 6892–6893.

27 Y. Matsunaga, N. Miyajima, Y. Nakayasu, S. Sakai, M. Yonenaga, *Bull. Chem. Soc. Jpn.* **1988**, *61*, 207–210.

28 P. J. M. Stals, M. M. J. Smulders, R. Martín-Rapún, A. R. A. Palmans, E. W. Meijer, *Chem. Eur. J.* **2009**, *15*, 2071–2080.

29 S. Cantekin, T. F. A. de Greef, A. R. A. Palmans, *Chem. Soc. Rev.* **2012**, *41*, 6125–6137.

30 C. F. C. Fitié, E. Mendes, M. A. Hempenius, R. P. Sijbesma, *Macromolecules* **2011**, *44*, 757–766.

31 T. Q. Nguyen, M. L. Bushey, L. E. Brus, C. Nuckolls. *J. Am. Chem. Soc.* **2002**, *124*, 15051–15054.

32 M. L. Bushey, A. Hwang, P. W. Stephens, C. Nuckolls, *Angew. Chem. Int. Ed.* **2002**, *41*, 2828–2831.

33 A. V. Gorbunov, T. Putzeys, I. Urbanavičiūtė, R. A. J. Janssen, M. Wübbenhorst, R. P. Sijbesma, M. Kemerink, *Phys. Chem. Chem. Phys.* **2016**, *18*, 23663–23672.

34 Müllen, K., Reynolds, J. R., Masuda, T., Eds. Conjugated Polymers, Royal Society of Chemistry: Cambridge, **2013**.

35 Skotheim, T. A. Handbook of Conducting Polymers, 2nd ed.; CRC Press: Boca Rotan, FL, **1997**.

36 Frank, A. J. In Energy Resources Through Photochemistry and Catalysis, M. Grätzel, Ed.; Academic Press: New York, **1983**, pp 467–505.

37 P. G. Pickup, R. A. Osteryoung. *J. Am. Chem. Soc.* **1984**, *106*, 2294–2299.

38 A. F. Diaz, K. K. Kanazawa, G. P. Gardini. *J. Chem. Soc. Chem. Commun.* **1979**, 635–636.

39 A. F. Diaz, J. I. Castillo, J. A. Logan, W. Y. Lee. *J. Electroanal. Chem. Interfacial Electrochem.* **1981**, *129*, 115–132.

40 G. B. Street, T. C. Clarke, R. H. Geiss, V. Y. Lee, A. Nazzal, P. Pfluger, J. C. Scott. *J. Phys. Colloq.* **1983**, *44*, C3-599–C3-606.

41 G. Zotti, S. Zecchin, G. Schiavon, B. Vercelli, A. Berlin, E. Dalcanale, L. Groenendaal. *Bert" Chem. Mater.* **2003**, *15*, 4642–4650.

42 Diaz, A. F., Kanazawa, K. K. In Extended Linear Chain Compounds, J. S. Miller, Ed.; Springer: New York, **1983**, pp 417–441.

43 Mohammad, F. In Handbook of Advanced Electronic and Photonic Materials and Devices; Academic Press: Burlington, **2001**; pp 321–350.

44 N. Azizi, A. Khajeh-Amiri, H. Ghafuri, M. Bolourtchian, M. Saidi, *Synlett* **2009**, *2009*, 2245–2248.

45 P. P. Bose, M. G. B. Drew, A. K. Das, A. Banerjee, *Chem. Commun.* **2006**, 3196–3198.

46 M. P. Lightfoot, F. S. Mair, R. G. Pritchard, J. E. Warren, *Chem. Commun.* **1999**, 1945–1946.

47 I. A. W. Filot, A. R. A. Palmans, P. A. J. Hilbers, R. A. van Santen, E. A. Pidko, T. F. A. de Greef, *J. Phys. Chem. B.* **2010**, *114*, 13667–13674.

48 A. Rochefort, É. Bayard, S. Hadj-Messaoud. *Adv. Mater.* **2007**, *19*, 1992–1995.

49 T. Shikata, Y. Kuruma, A. Sakamoto, K. Hanabusa, *J. Phys. Chem. B.* **2008**, *112*, 16393–16402.

50 R. Q. Albuquerque, A. Timme, R. Kress, J. Senker, H. W. Schmidt, *Chem. Eur. J.* **2013**, *19*, 1647–1657.

51 H. Steininger, M. Schuster, K. D. Kreuer, A. Kaltbeitzel, B. Bingöl, W. H. Meyer, S. Schauff, G. Brunklaus, J. Maier, H. W. Spiess, *Phys. Chem. Chem. Phys.* **2007**, *9*, 1764–1773.

52 S. Sadki, P. Schottland, N. Brodie, G. Sabouraud, *Chem. Soc. Rev.* **2000**, *29*, 283–293.

53 W. Cui, Z. Xia, S. Wu, F. Chen, Y. Li, B. Sun, *ACS Appl. Mater. Interfaces* **2015**, *7*, 25601–25607.

54 J. Grondin, D. Rodriguez, J. C. Lassègues, *Solid State Ionics* **1995**, *77*, 70–75.

55 K. Asadi, J. Wildeman, P. W. M. Blom, D. M. de Leeuw, *IEEE Trans. Electron Devices* **2010**, *57*, 3466–3471.

56 The thickness of the layer of oxidized material can be estimated from the charge density corresponding to the electrochemical process without the ferroelectric switching current. When taking into account the volume of a single molecule (from the unit cell in XRD), the charge of the electron and the production of 6 protons per fully oxidized molecule with 3 pyrrole units, the thickness of polymerized material on each electrode is calculated to be approximately 17 nm after 21 h. of cycling. For a detailed calculation, see SI.